Journal of Materials Chemistry A

PAPER

View Article Online
View Journal | View Issue

Cite this: J. Mater. Chem. A, 2016, 4, 18899

Vanadium pentoxide/carbide-derived carbon core–shell hybrid particles for high performance electrochemical energy storage†

Marco Zeiger,[ab] Teguh Ariyanto,[c] Benjamin Krüner,[ab] Nicolas J. Peter,[d] Simon Fleischmann,[b] Bastian J. M. Etzold*[ce] and Volker Presser*[ab]

Received 13th October 2016
Accepted 31st October 2016

DOI: 10.1039/c6ta08900c

www.rsc.org/MaterialsA

A novel, two step synthesis is presented combining the formation of carbide-derived carbon (CDC) and redox-active vanadium pentoxide (V_2O_5) in a core–shell manner using solely vanadium carbide (VC) as the precursor. In a first step, the outer part of VC particles is transformed to nanoporous CDC owing to the *in situ* formation of chlorine gas from $NiCl_2$ at 700 °C. In a second step, the remaining VC core is calcined in synthetic air to obtain V_2O_5/CDC core–shell particles. Materials characterization by means of electron microscopy, Raman spectroscopy, and X-ray diffraction clearly demonstrates the partial transformation from VC to CDC, as well as the successive oxidation to V_2O_5/CDC core–shell particles. Electrochemical performance was tested in organic 1 M $LiClO_4$ in acetonitrile using half- and asymmetric full-cell configuration. High specific capacities of 420 mA h g^{-1} (normalized to V_2O_5) and 310 mA h g^{-1} (normalized to V_2O_5/CDC) were achieved. The unique nanotextured core–shell architecture enables high power retention with ultrafast charging and discharging, achieving more than 100 mA h g^{-1} at 5 A g^{-1} (rate of 12C). Asymmetric cell design with CDC on the positive polarization side leads to a high specific energy of up to 80 W h kg^{-1} with a superior retention of more than 80% over 10 000 cycles and an overall energy efficiency of up to 80% at low rates.

1. Introduction

Supercapacitors are electrochemical energy storage devices, which present ultrafast charge–discharge rates leading to higher power compared to conventional batteries, but suffer from relatively low specific energies.[1–4] The high specific power of ~10 kW kg^{-1} benefits applications with charge- and discharge rates in the order of seconds and minutes, such as flashlights, high power machinery, or emergency doors in airplanes, to name just a few.[2,5] Depending on the energy storage mechanism, we can differentiate between two types of supercapacitors, namely electrical double-layer capacitors (EDLCs) that store energy by ion electrosorption, and pseudocapacitors that accomplish a capacitor-like charge-voltage behavior by fast redox reactions.[6] Today, most EDLCs employ activated carbon (AC) electrodes with surface areas between 1500 and 2000 m^2 g^{-1}, leading to typical capacitance values of 100–200 F g^{-1} and specific energies of up to *ca.* 20 W h kg^{-1}, depending on the electrolyte and the cell configuration.[6] By virtue of these values, the energy storage capacity of supercapacitors is significantly smaller than conventional batteries (*e.g.*, lithium ion batteries: >100 W h kg^{-1}).[6] A facile way to enhance the electrochemical performance is to increase the specific surface area of the electrode material and to optimize the pore size distribution.[7] This is particularly effective for a material with very high pore tunability, as presented in the case of carbide-derived carbons (CDCs).[8] However, this strategy is limited by the minimum pore size required for ion accessibility and the charge screening ability of carbon.[7,9,10] Further enhancements of the energy storage capacity can be accomplished by employing redox-active materials for faradaic charge transfer.[11,12] The latter can be either in the form of fast redox processes of surface groups, ion intercalation in the electrode material, or redox reactions of the electrolyte.[13,14] Depending on the charge-voltage profile of the involved faradaic reaction(s), one differentiates between capacitor-like (*i.e.*, pseudocapacitive) or battery-like behavior.[15] Pseudocapacitive materials, exhibiting a constant ratio of charge and voltage (*i.e.*, capacitance, unit: farad), are, for example, ruthenium oxide,[16] manganese oxide,[17] or MXene.[18] Battery-like systems, exhibiting distinct redox peaks

[a]INM – Leibniz Institute for New Materials, 66123 Saarbrücken, Germany. E-mail: volker.presser@leibniz-inm.de
[b]Department of Materials Science and Engineering, Saarland University, 66123 Saarbrücken, Germany
[c]Friedrich-Alexander Universität Erlangen-Nürnberg, Lehrstuhl für Chemische Reaktionstechnik, 91058 Erlangen, Germany
[d]Max-Planck Institut für Eisenforschung GmbH, 40237 Düsseldorf, Germany
[e]Technische Universität Darmstadt, Ernst-Berl-Institut für Technische und Makromolekulare Chemie, 64287 Darmstadt, Germany. E-mail: etzold@tc1.tu-darmstadt.de

† Electronic supplementary information (ESI) available. See DOI: 10.1039/c6ta08900c

in the cyclic voltammogram, are, for example, quinone surface groups[19,20] or many metal oxides working as cathodic lithium-intercalation hosts (such as $LiFePO_4$, $LiCoO_2$, $LiMn_2O_4$, and $LiFeSO_4F$; ref. 21).

A very promising electrochemical system employs the hybridization of carbon materials with vanadium pentoxide (V_2O_5).[22–26] By this way, the beneficial electrical conductivity and nanotextured surface of carbon is complemented by the high, battery-like charge storage capacity of vanadia with a theoretical capacity of 147 mA h g^{-1} for intercalation of 1 M of Li in the V_2O_5 structure.[27] Several studies have investigated vanadium pentoxide as a cathode material in lithium ion batteries, exhibiting high capacities between 350 and 750 mA h g^{-1}.[28–30] Furthermore, other types of vanadia in different oxidation states can be used in batteries, such as VO_2,[31] and also dissolved as an electrolyte in redox-flow batteries.[32] In a previous study, we used atomic layer deposition (ALD) for highly controllable decoration of carbon onions with V_2O_5, achieving defined thickness, morphology, and crystallinity of the metal oxide phase.[33] A high specific energy (38 W h kg^{-1}) was achieved for a full-cell using V_2O_5/carbon onion *vs.* activated carbon (asymmetric cell), which is *ca.* 2-times higher than that of standard activated carbon in organic electrolytes.[33] Even higher values for the specific energy were found for interpenetrating networks of CNTs and V_2O_5 nanowires (40 W h kg^{-1})[22] and vanadia-coated reduced graphene oxide sheets (76 W h kg^{-1}).[34] While promising, the practical adaptation of microfabrication and ALD remains limited and more facile synthesis routes for V_2O_5/carbon hybrid materials remain in high demand.

The combination of redox-active metal oxides with conductive and porous carbons in a hybrid device can be achieved by mechanical mixing (thus exhibiting strongly reduced conductivity), or the decoration of the carbon with metal oxides. For the latter, especially when using highly porous carbons, issues of pore clogging may arise, leading to a strong decrease in capacitance and specific energy. These complications are avoided by not coating the carbon with the metal oxide, but rather fabricating a metal oxide core with a porous carbon shell. Inspired by carbon only core–shell architectures, which can be obtained for CDCs,[35,36] we present a novel two-step synthesis for V_2O_5/CDC composites in a core–shell arrangement. Our approach requires only one precursor (vanadium carbide), which is first partially transformed to nanoporous CDC by chlorine treatment of carbide, and then partially calcined, yielding core–shell V_2O_5/CDC particles. The chlorination step was needed as it is an effective way to transform a metal carbide to carbon. The nanoporous carbon shell makes the vanadium pentoxide core accessible for ion intercalation and works as a conductive additive. This was accomplished by a high level of control over the synthesis steps, which prevented a completion of both the chlorination and the oxidation processes. Rigorous structural and electrochemical characterization was carried out to establish the high energy storage capacity of the material in organic electrolytes. The combination of carbon and vanadia is of mutual benefit: carbon contributes electrical conductivity (and, to a lesser extent, double-layer capacitance) and vanadia provides a large energy storage capacity. However, the design of the two phases and their nanoscopic arrangement are of high importance for the resulting electrochemical performance. As our data will show, the firm of transformed VC-derived V_2O_5 and VC-CDC enables attractive electrochemical performances.

2. Materials and methods

V_2O_5/porous carbon core–shell particles were synthesized using a two-step approach: (1) VC/CDC core–shell particles are produced by etching vanadium from the outside to the inside of VC particles with a remaining VC core. (2) The residual VC core inside the CDC matrix is calcined by oxidation in synthetic air, resulting in V_2O_5/CDC core–shell particles. These two steps are explained in detail in the next sections.

2.1 Synthesis of vanadium carbide/carbide-derived carbon core–shell particles

Vanadium carbide (VC)/CDC core–shell particles were synthesized by reactive extraction of vanadium using *in situ* generation of chlorine. 1 g VC powder (purity 99.9%, <2 μm, Sigma Aldrich) was thoroughly mixed with $NiCl_2 \cdot 6H_2O$ (purity 99.95%, Alfa Aesar) and filled into a graphite crucible placed in an isothermal zone of the reactor (Ø = 32 cm, length = 1 m). The reactor was evacuated to 0.01 mbar and then heated to 700 °C at a heating rate of 2.5 °C min^{-1}. After a holding period of 3 h at this temperature, the reactor was cooled to room temperature under a helium purge. The resulting product was then poured into 500 mL of 1 M HCl and the solution was vigorously stirred using a magnetic stir bar. After filtration, the acid washing was repeated with similar procedures to ensure the removal of nickel species. The product was finally washed using distilled water until neutral pH and then dried in an oven (60 °C) overnight.

To achieve incomplete carbide-to-CDC conversion, we used molar ratios of $NiCl_2 \cdot 6H_2O$-to-VC of 1.4, 1.8, and 2.7. It is assumed that chlorine (Cl_2) is released during vacuum decomposition of $NiCl_2$ and reacts with VC in a stoichiometric reaction to produce VCl_4 *via* eqn (1) and (2).

$$[NiCl_2 \cdot 6H_2O]^{solid} \rightarrow [Ni]^{solid} + [Cl_2]^{gas} + [6H_2O]^{gas} \quad (1)$$

$$[VC]^{solid} + [2Cl_2]^{gas} \rightarrow [C]^{solid} + [VCl_4]^{gas} \quad (2)$$

Based on these reactions and assuming that all chlorine reacts with carbide the theoretical conversion ($X_{theo.}$) can be derived from eqn (3) assuming full reaction of VC with Cl_2 release.

$$X_{theo.} = \frac{0.5 n_{Cl_2}}{n_{VC}} \times 100\% = \frac{0.5 n_{NiCl_2 \cdot 6H_2O}}{n_{VC}} \times 100\% \quad (3)$$

where n is in molar units. Ratios of 1.4 and 1.8 correspond to a theoretical value ($X_{theo.}$) of the conversion of 70% and 90%, respectively. A ratio of 2.7 provides a surplus of evolving chlorine to facilitate complete CDC formation, theoretically 100%. The resulting samples are labelled VC-X70, VC-X90, and VC-X100.

To produce a reference material through the "classical" and not *in situ* chlorine generation route, VC was exposed to chlorine gas diluted in helium at 700 °C for 5 h, as described elsewhere.[63] The resulting material is labelled VC-CDC.

2.2 Synthesis of V_2O_5/carbide-derived carbon core–shell particles

Calcination of the VC/CDC particles was performed at 450 °C for 30 min in a VG Scienta furnace using synthetic air. Additionally, VC particles without prior chlorine gas treatment were oxidized at different temperatures (450, 500, and 600 °C) for 4 h to produce V_2O_5 without an additional carbon shell.

2.3 Chemical and structural characterization

The chemical composition of all samples was measured by energy-dispersive X-ray analysis (EDX) using a X-Max-150 detector from Oxford Instruments in a JSM-7500F (JEOL) scanning electron microscope. Spectra were taken at ten different positions with an acceleration voltage of 10 kV.

Transmission electron microscopy (TEM) was carried out with a JEOL 2100F microscope using 200 kV acceleration voltage. Powders were dispersed in isopropanol, tip sonicated for 10 s and dropcast on a copper grid with a lacey carbon film (Gatan) support.

Chemical composition maps were acquired by energy filtered transmission electron microscopy (EF-TEM) using a FEI Titan Themis 60-300 at an acceleration voltage of 300 kV. Electron energy loss spectra (EELS) were recorded using a Gatan GIF Quantum ERS energy filter at an energy resolution of ~1.1 eV. From the acquired EELS the edge onsets of the carbon K-edge, the vanadium L-edge and the oxygen K-edge were determined and the three-window method applied to acquire the respective elemental maps. A slit width of 10 eV was utilized for the pre- and post-edge images. Since the vanadium and oxygen edges overlap, the exact same pre-edge windows were taken for both images. More information can be found in the ESI.†

Thermogravimetric analysis (TGA) was carried out with a TG 209 F1 Libra system (Netzsch). Samples were heated up to 900 °C in synthetic air with a rate of 20 °C min^{-1} as well as isothermally at 450 °C for 30 min. The sample mass ranged between 10 mg and 20 mg.

The nitrogen gas sorption analysis at −196 °C was carried out with a Quantachrome Autosorb iQ system and the calculations were performed with ASiQwin-software 3.0. The samples were degassed at 100 °C for 1 h and subsequently heated to 150 °C and kept at this temperature for up to 20 h at a relative pressure of 0.1 Pa to remove volatile molecules from the surface. The relative pressure with nitrogen was 5×10^{-7} to 1.0 in 76 steps. The specific surface area (SSA) was calculated using the Brunauer–Emmett–Teller equation (BET) in the linear regime of the measured isotherms, typically 3×10^{-2} to 2×10^{-1} (relative pressure), with a Quantachrome Autosorb 6B.[64]

Raman spectra were recorded with a Renishaw inVia Raman Microscope equipped with a Nd–YAG laser (532 nm). A 50× objective was used with a power of 0.02 mW at the surface of the sample. The spectra of CDC samples were recorded with 10 accumulations and 20 s acquisition time. Vanadium pentoxide and vanadium carbide spectra were recorded with 1 accumulation and 10 s acquisition as well as in two separate measurements for the full wavenumber range (0–4000 cm^{-1}). All spectra were normalized and background corrected by subtracting a linear baseline.

X-ray diffractograms were collected with a Bruker D8 Discover diffractometer using Cu-K_α radiation (0.154 nm) with a step size of 0.02° and a measurement time of 1 s per step. The system was calibrated with a corundum standard. The free-standing PTFE-bound electrodes were placed on a sapphire single crystal for the measurement.

2.4 Electrochemical characterization

For electrochemical characterization, free-standing, polymer-bound electrodes were used. The powder materials were dispersed in isopropanol and stirred in a mortar until most of the isopropanol was evaporated and a carbon slurry was obtained. For all samples, 10 mass% PTFE (60 mass% aqueous solution, Sigma Aldrich) was added and mixed in a mortar until a dough-like paste was formed. For the electrodes with pure V_2O_5 (VC-500) an additional conductive additive (see also the ESI, Table S1†), in this case 25 mass% VC-CDC was added to achieve the same amount of carbon as in the core–shell electrodes. Using a rolling machine (MTI HR01, MTI Corp.) electrodes with a thickness of 60 μm (±10 μm) were fabricated and dried overnight at 90 °C and 20 mbar.

Electrochemical characterization was carried out in 1 M $LiClO_4$ in acetonitrile (ACN) from BASF. For all measurements, a two- and three-electrode setup was used, corresponding to full- and half-cell configuration, respectively. The electrodes were punched out to obtain discs with a diameter of 6 mm (1–3 mg) and were separated by a glass-fiber disc with a diameter of 13 mm (type GF/A, GE Healthcare). The electrode/separator/electrode arrangement was compressed between two carbon-coated aluminum discs (diameter 12 mm, type Zflo 2653, Coveris Advanced Coatings) using spring-loaded titanium pistons, sealed by a polyether ether ketone (PEEK) body. The cells were dried at 90 °C and 20 mbar before they were put in an argon-filled glove box (MBraun Labmaster 130; O_2, H_2O <1 ppm). The cells were vacuum back-filled with a syringe containing the electrolyte. Full-cell measurements were carried out in an asymmetric configuration with a charge-balanced counter VC-CDC electrode by measuring the discharge capacity at 0.05 A g^{-1} in a half-cell setup for both, working and counter electrodes, and adjusting the mass of the VC-CDC electrode. In the half-cell setup, a *ca.* five times oversized AC counter electrode was used together with a reference electrode; the latter was PTFE-bound activated carbon YP-50F from Kuraray.

Electrochemical characterization was performed using a VSP300 and VMP300 potentiostat/galvanostat from Bio-Logic in cyclic voltammetry (CV) and galvanostatic mode with potential limitation (GCPL). In the half-cell configuration a potential window from −1.2 V to +1.2 V *vs.* carbon was used. For data obtained with cyclic voltammetry, a scan rate of 1 mV

s^{-1} was chosen to clearly identify the redox peaks. In galvanostatic mode with potential limitation (GCPL), specific currents up to 20 A g^{-1} were applied. All specific current values were normalized to the active mass of the working electrode (*i.e.*, without the binder). Every cycle was repeated 2 times, followed by a 10 s resting time. The specific capacity of the working electrode in the half-cell configuration was calculated according to eqn (4), using the data from GCPL.

$$\text{Specific capacity} = \int_{t_1}^{t_2} I\,\mathrm{d}t \Big/ m \tag{4}$$

with m the active mass of the working electrode (*i.e.*, without the binder), I the applied current, and t_1 and t_2 the start and end of discharging (from +1.2 V to −1.2 V *vs.* carbon), respectively. The charge efficiency was calculated by dividing the discharge by the charge capacity and is presented in percent.

The specific energy (E_{specific}) and specific power (P_{specific}) of the asymmetric full-cells (two electrodes) were calculated using eqn (5) and (6):

$$E_{\text{specific}} = \int_{t_1}^{t_2} U\,\mathrm{d}t \times I/M \tag{5}$$

$$P_{\text{specific}} = E_{\text{specific}}/(t_2 - t_1) \tag{6}$$

with M the active mass of both electrodes (*i.e.*, without the binder), I the applied current, U the applied cell voltage, t_1 and t_2 the start and end of charging or discharging. Charging is in this case defined as the potential step from 0 V to 2.5 V cell voltage.

Long-time stability was measured by galvanostatic cycling at 1 A g^{-1} from 0 V to 2.5 V cell voltage for 10 000 times. The energy efficiencies, as well as the energy retention, were calculated dividing the respective value from discharging by the value from the charging part of the curve and are presented in percent.

3. Results and discussion

3.1 Structure, chemical composition, and porosity

In this study, a novel two-step process is presented, which can be used for the synthesis of vanadium oxide combined with porous carbide-derived carbon hybrid structures in a core–shell arrangement: (1) VC/CDC core–shell particles are produced by etching vanadium from the outside to the inside of VC particles with a remaining VC core. (2) The residual VC core inside the CDC matrix is calcined by oxidation in synthetic air, resulting in V_2O_5/CDC core–shell particles. The resulting samples are labelled VC-X70, VC-X90, and VC-X100 for a theoretical conversion of 70%, 90%, and 100%. For additional calcination the samples were labelled VC-X70-air, VC-X90-air, and VC-X100-air. Complete transformation from VC to CDC (*i.e.*, VC-CDC) was achieved by conventional chlorine gas treatment at 700 °C, resulting in highly disordered carbon (Fig. 1A). Minor amounts of VC are still visible in VC-CDC (Fig. 1A) but not quantitatively significant according to the chemical analysis (Table 1). For the synthesis of VC/CDC core–shell particles with different ratios of VC to CDC, the amount of $NiCl_2$ was varied for *in situ* chlorine formation during thermal treatment. As expected from the stoichiometric calculation presented in eqn (3), VC-X70 had the largest amount of VC in the composite with 40.2 ± 5.3 mass%. Larger amounts of $NiCl_2$ led to lower VC contents of 29.0 ± 7.5 mass% and 6.9 ± 2.4 mass% for VC-X90 and VC-X100, respectively (Table 1). Although a stoichiometric surplus of chlorine in VC-X100 should result in complete transformation to CDC, TEM analysis still shows a small core region of residual VC. We explain this by a reduced vanadium etching rate because of the graphitic carbon layers wrapped around the carbide domains.[37]

A calcination temperature of 450 °C was chosen to completely transform residual VC to vanadium oxide after initial benchmarking of the samples *via* thermogravimetric analysis (see the ESI, Fig. S1†). After calcination, vanadium oxide cores inside the carbon shell are clearly visible (Fig. 1D, G and J). The smallest vanadia cores are measured for VC-X100-air (d_{50} = 150 ± 100 nm), similar to VC-X90-air (d_{50} = 160 ± 110 nm), much smaller than for VC-X70-air (d_{50} = 410 ± 190 nm) and the calcined VC particles (VC-500 °C) (d_{50} = 520 ± 200 nm). As seen in Table 1, EDX measurements are in qualitative agreement with TEM and show V_2O_5 contents of 98.1 ± 6.2 mass% for the precursor VC particles oxidized at 500 °C and lower amounts from 78.2 ± 2.3 mass% for VC-X70-air to 67.4 ± 4.1 mass% for VC-X100-air.

To show the structure and morphology in more detail, the two step synthesis process is illustrated in Fig. 2 using energy filtered TEM (EF-TEM) based chemical mapping. As exemplified for VC, VC-X90, and VC-X90-air, we first see how VC particles were successively transformed to CDC from the outside to the inside retaining a VC core. Calcination of VC inside the composite particles leads to V_2O_5 domains engulfed in nanoporous VC-CDC. EF-TEM chemical mapping confirms the distribution of carbon around the V_2O_5. During calcination, a partial cracking of the carbon shell is induced due to expansion of the core, as a result of the different skeletal densities of 3.36 g cm^{-3} for V_2O_5 and 5.48 g cm^{-3} for VC.[38,39]

By use of Raman spectroscopy, we can track the structural changes after CDC synthesis (Fig. 3A) and calcination (Fig. 3C). It is shown that the VC signal intensity at 269 cm^{-1} decreases with successive transformation from VC to CDC (see the inset in Fig. 3A).[40] In addition to the VC signal, the Raman spectra show incompletely graphitized carbon, with the D-mode at *ca.* 1340–1350 cm^{-1}, the G-mode at *ca.* 1580–1600 cm^{-1}, and a pronounced second order spectrum at 2200–3500 cm^{-1}. The degree of carbon ordering in VC/CDC core–shell particles is significantly higher than for the fully transformed CDC by chlorine treatment (VC-CDC). This is evidenced by the broader peak shapes and transition between D- and G-mode due to amorphous carbon at ~1520 cm^{-1}, as well as the less distinct second order spectrum for the VC-CDC sample (Fig. 3A).[41,42] However, the process stemming from $NiCl_2$ also leads to the local emergence of metallic Ni, which, in turn, catalyzes the formation of graphitic carbon arranged in onion-like shells (Fig. 1I and J).[43]

As seen from Fig. S1 (ESI†), precise control over the calcination process temperature and duration is required to avoid

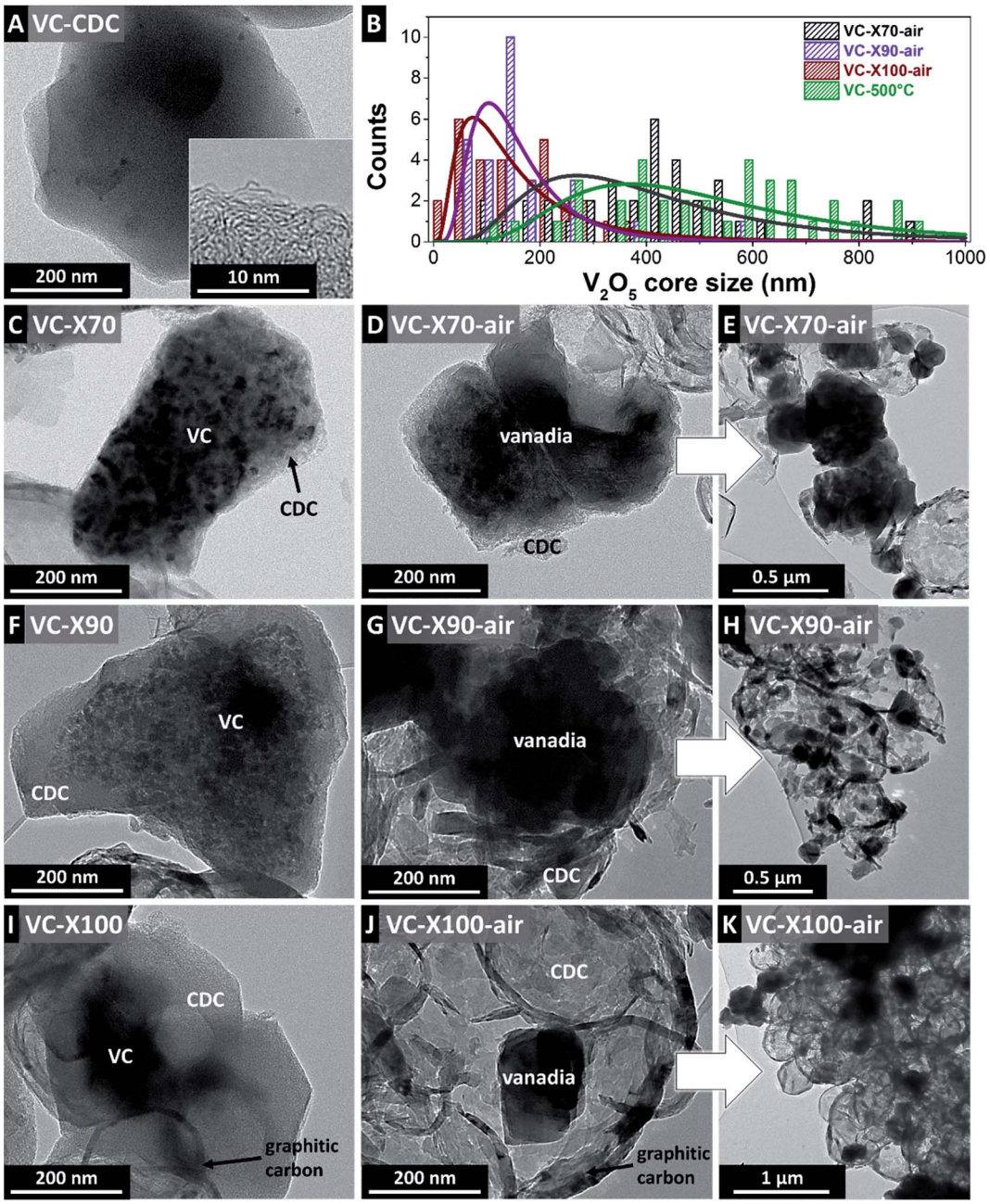

Fig. 1 Transmission electron micrographs of the transformation process from VC to V_2O_5/CDC core–shell particles with different transformational degrees. (A) VC-CDC, (C–E) VC-X70 and VC-X70-air, (F–H) VC-X90 and VC-X90-air, and (I–K) VC-X100 and VC-X100-air. (B) V_2O_5 core diameter distributions derived from TEM image analyses for all calcined samples.

either incomplete carbide oxidation or complete CDC burn-off. For this reason, we conducted first oxidation experiments only on the initial VC powder. The increase in mass of the initial VC particles, without prior $NiCl_2$ treatment, is ~40 mass% (ESI, Fig. S1†) for an annealing at 600 °C, leading to crystalline V_2O_5 (Fig. 3B). However, using this calcination temperature, more than 50 mass% of the CDC was burned-off. Therefore, the synthesis was repeated at a lower temperature of 450 °C for a duration of 30 min. With this annealing process, the same mass increase (~40 mass%) was achieved, expecting the same vanadia phase, and only ~20 mass% of the CDC material was removed. Synthesis at 450 °C for 30 min results in a mixture of V_2O_5,[44] amorphous V_2O_5,[45] and VO_2 (ref. 46) because of the large size of the precursor VC particles (~1 µm) (Fig. 3B). The particles with the VC/CDC core–shell arrangement present much smaller cores than the initial VC particles (Fig. 1B), which leads to the formation of V_2O_5 already at 450 °C applied for 30 min (Fig. 3C). These findings are supported by X-ray diffraction (XRD), shown in the ESI, Fig. S2.† Transformation from VC to VC/CDC is clearly evidenced by the emergence of the (002) graphite signal at 26.4° 2θ for VC-X70 and the continuous increase of its intensity up to the highest degree of

Table 1 Elemental composition measured with EDX. "n.d." denotes not detected

	C (mass%)	V (mass%)	O (mass%)	Cl (mass%)	Ni (mass%)	VC (mass%)	V_2O_5 (mass%)
VC	22.0 ± 0.5	77.6 ± 0.7	n.d.	n.d.	n.d.	95.9 ± 1.1	
VC-X70	60.6 ± 4.1	32.5 ± 4.7	6.3 ± 1.1	0.6 ± 0.1	n.d.	40.2 ± 5.3	
VC-X90	58.2 ± 9.5	23.5 ± 7.1	6.9 ± 2.1	0.5 ± 0.2	n.d.	29.0 ± 7.5	
VC-X100	74.8 ± 8.0	5.6 ± 2.3	4.5 ± 0.9	0.4 ± 0.1	n.d.	6.9 ± 2.4	
VC-CDC	97.8 ± 0.4	0.2 ± 0.1	1.8 ± 0.5	0.1 ± 0.1	n.d.	0.2 ± 0.1	
VC-500	1.9 ± 0.4	69.0 ± 3.2	29.1 ± 3.0	n.d.	n.d.		98.1 ± 6.2
VC-X70-air	20.0 ± 2.2	57.9 ± 1.1	22.1 ± 1.2	n.d.	n.d.		78.2 ± 2.3
VC-X90-air	23.3 ± 5.4	53.3 ± 4.2	22.8 ± 2.0	n.d.	0.6 ± 0.2		74.3 ± 6.2
VC-X100-air	30.7 ± 1.7	48.5 ± 2.4	20.7 ± 1.7	n.d.	n.d.		67.4 ± 4.1

transformation for VC-X100 (ESI, Fig. S2A†). The fully transformed VC-CDC presents a less distinct carbon signal, coming from nanocrystalline and amorphous carbon, in agreement with Raman spectroscopy. After calcination, only V_2O_5 is identified (ESI, Fig. S2B†).

Highly nanoporous materials with high specific surface areas typically result from chlorine treatment of VC (*i.e.*, VC-CDC).[38] The nitrogen gas sorption isotherm of VC-CDC shows a characteristic type I(b) shape related to microporous materials with pore sizes <2.5 nm (ESI, Fig. S3A†). Both micro- and mesopores are found for the partial transformation of VC with type I(b) isotherms, related to the internal microporosity, combined with type IV(b) isotherms related to mesopores with a small H4 hysteresis (Fig. S3B†).[47] The combination of micro- and mesopores has been reported in other studies on carbon core–shell structures.[36] The BET surface area increases from 120 $m^2 g^{-1}$ for VC-X70 to 577 $m^2 g^{-1}$ for VC-X100, and to 1466 $m^2 g^{-1}$ for VC-CDC (Table 2). Calcination of VC/CDC core–shell particles does not change the pore type (micro- and mesopores), but leads to oxidation of the high surface area carbon, with consequent decrease in surface area. For VC-X100-air and VC-X90-air, the surface area collapses to 61 $m^2 g^{-1}$ (−89%) and 124 $m^2 g^{-1}$ (−38%), respectively, due to oxidation of the CDC shell. The surface area of VC-X70-air is even larger than before calcination with 310 $m^2 g^{-1}$ (+158%; Table 2). The high content of VC in VC-X70 (40 mass%), which is turned into the lower density V_2O_5, has a stronger impact on the surface area than the CDC, compared to VC-X90 and VC-X100 with lower VC contents.

3.2 Electrochemical performance

As seen from the previous section, partial chlorination of VC to VC/CDC and successive calcination to V_2O_5/CDC in a facile two-step approach leads to highly crystalline V_2O_5 embedded graphitic and porous carbon. This combination is promising for electrochemical hybrid energy storage applications, which was benchmarked in our study in 1 M $LiClO_4$ in ACN as the electrolyte. Cyclic voltammetry of VC-CDC using the half-cell setup shows a nearly ideal double-layer capacitor behavior with a rectangular CV shape without any redox reactions. This behavior is expected from nanoporous carbons in general and CDC materials in specific.[6] VC-X70-air is characterized by double-layer capacitance on the positive side between +0.5 V and +1.2 V *vs.* carbon. In the negative range, a very broad redox peak emerges (Fig. 4B and ESI, Fig. S4B†). This broad peak correlates with the larger V_2O_5 core of VC-X70 compared to the nanotextured V_2O_5 particles in VC-X90-air and VC-X100-air. Due to longer ion pathways in the V_2O_5 crystal, the system presents slower redox reactions and broader redox peaks.

In stark contrast to the capacitor-like behavior of VC-CDC, the CVs of VC-X90-air and VC-X100-air are characterized by several, very sharp redox peaks from Li-ion intercalation.[30,48,49] The occurring electrochemical Li^+ insertion process for V_2O_5 can be expressed by eqn (7):[50]

$$V_2O_5 + xLi^+ + xe^- \leftrightarrow Li_xV_2O_5 \quad (7)$$

with x as the mole fraction of Li-ions.

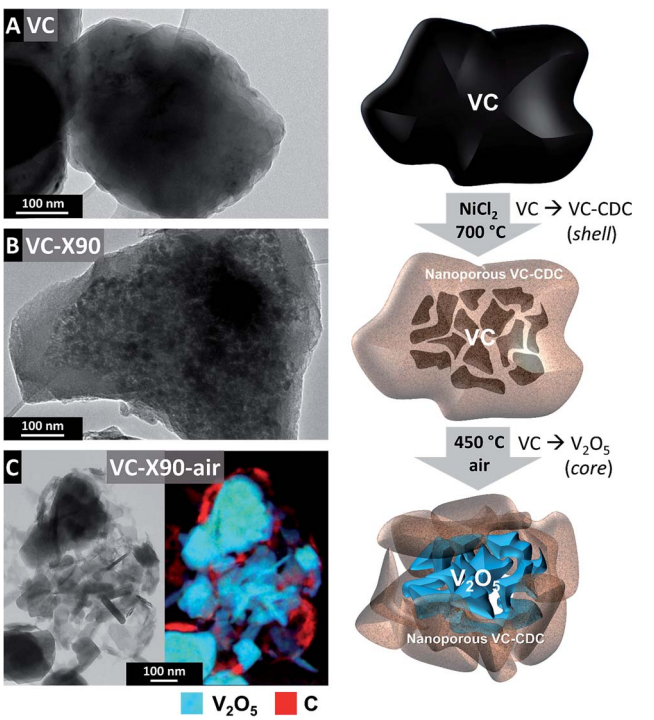

Fig. 2 Transmission electron micrographs and schematic illustration of the transformation process from VC to V_2O_5/CDC core–shell particles. (A) VC, (B) VC-X90, and (C) VC-X90-air. Panel (C) shows the TEM image (filtered ±5 eV around the zero loss peak) and the corresponding chemical EELS mapping.

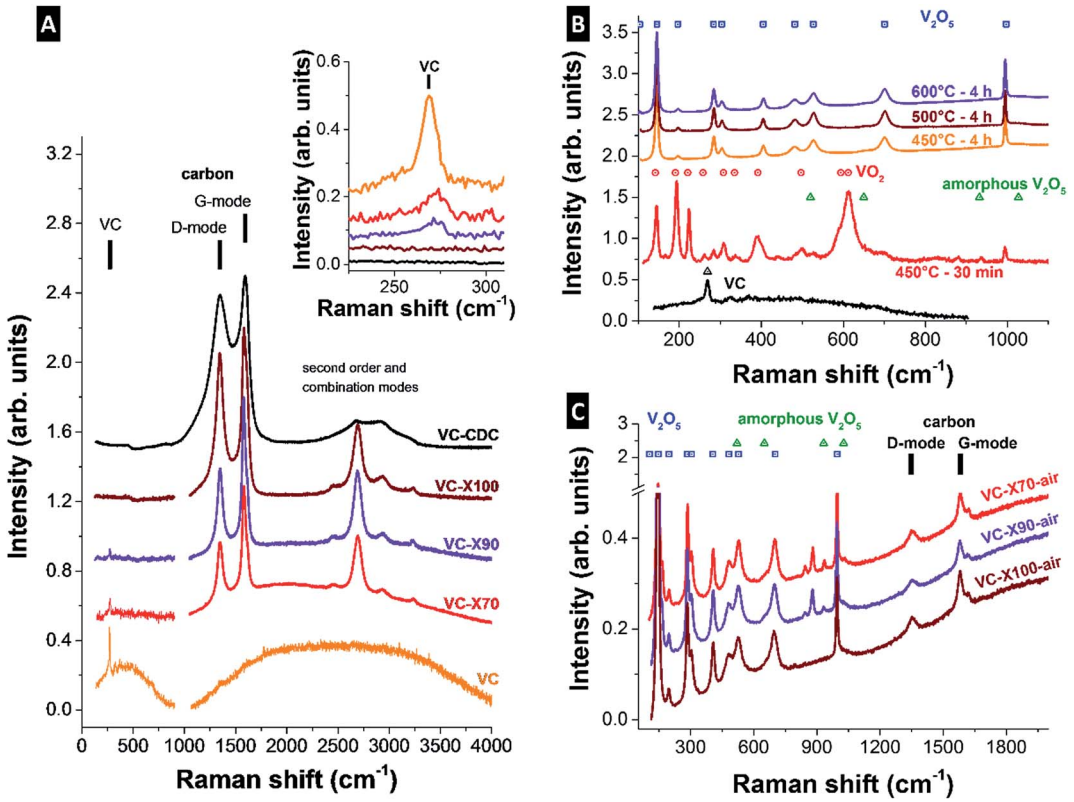

Fig. 3 Raman spectra of (A) VC and VC/CDC core–shell particles, (B) VC calcined at different temperatures, and (C) V_2O_5/CDC core–shell particles after calcination at 450 °C for 30 min. The reference Raman peaks are from VC,[40] VO_2,[46] V_2O_5,[44] and amorphous V_2O_5.[45]

Typically, a set of two peaks for inter- and deintercalation is observed between +2 and +4 V *vs.* Li/Li^+ or −1.2 V and +0.8 V *vs.* carbon.[48] The structural changes during Li^+ intercalation into V_2O_5 involve several phases like α, ε, δ, and γ for $x \leq 2$, with three voltage plateaus at 3.4, 3.2, and 2.3 V *vs.* Li/Li^+ (−0.7 V, 0 V, and +0.2 V *vs.* carbon) (Fig. 4B).[48] The plateaus seen from the galvanostatic curves (Fig. 4B) and the pairs of redox peaks in the CVs (Fig. 4A) belong to the two-phase regions α/ε, ε/δ, and δ/γ. Larger lithium contents ($x > 2$) for potentials below 2 V *vs.* Li/Li^+ (−1.2 V *vs.* carbon) would lead to irreversible reactions and the formation of the γ-phase.[48,51,52] A detailed discussion of the structural changes is already given in ref. 48 and 51–53. The first set of redox peaks emerges between −0.25 V and +0.8 V *vs.* carbon for inter- and deintercalation of the first Li-ion. A second lithiation step occurs between −1.2 V and 0 V *vs.* carbon (ESI, Fig. S4A†). For potentials above +0.8 V *vs.* carbon, only double-layer capacitance of the porous carbon is encountered. Calcined VC without the core–shell structure, but the same V_2O_5 phase, shows very broad sets of redox peaks in the CV compared to the core–shell structure. It is expected that longer ion intercalation paths of the larger size of V_2O_5 domains in VC-500 °C result in slower redox reactions of the electrode, similar to VC-X70-air. In contrast, the core–shell structures present much smaller V_2O_5 particles due to partial transformation into porous carbon.

Galvanostatic charge/discharge cycling (GCPL) in half-cells was further employed for assessing the power handling ability of the electrode materials. As seen from Fig. 4B, GCPL curves of VC-X100-air and VC-X90-air exhibited several voltage plateaus between −1.2 V and +1.2 V *vs.* carbon, in agreement with the redox peaks in the CVs. Nearly ideal double-layer behavior with triangular-shape GCPL curves was observed for VC-CDC. The Li^+ intercalation and deintercalation leads to phase transitions during cycling and is kinetically enhanced for nanoscopic materials because of better accessibility of intercalation pathways.[54] Therefore, smaller V_2O_5 core sizes of V_2O_5/CDC core–shell samples show superior rate handling compared to VC-500 with a more than 2-times larger V_2O_5 particle size (Fig. 4C). This is especially seen for VC-X100-air with more than 100 mA h g^{-1} capacity at 5 A g^{-1} (equivalent to a rate of *ca.* 28C).

The lower vanadium oxide content of VC-X100-air limits the maximum capacity at low rates. The highest value is achieved

Table 2 Porosity data from nitrogen gas sorption analysis

	BET SSA (m^2 g^{-1})	DFT SSA (m^2 g^{-1})	Pore volume (cm^3 g^{-1})
VC-X70	120	100	0.185
VC-X90	200	208	0.224
VC-X100	577	485	0.424
VC-CDC	1466	1535	0.673
VC-500	42	23	0.053
VC-X70-air	310	269	0.254
VC-X90-air	124	66	0.171
VC-X100-air	61	38	0.108

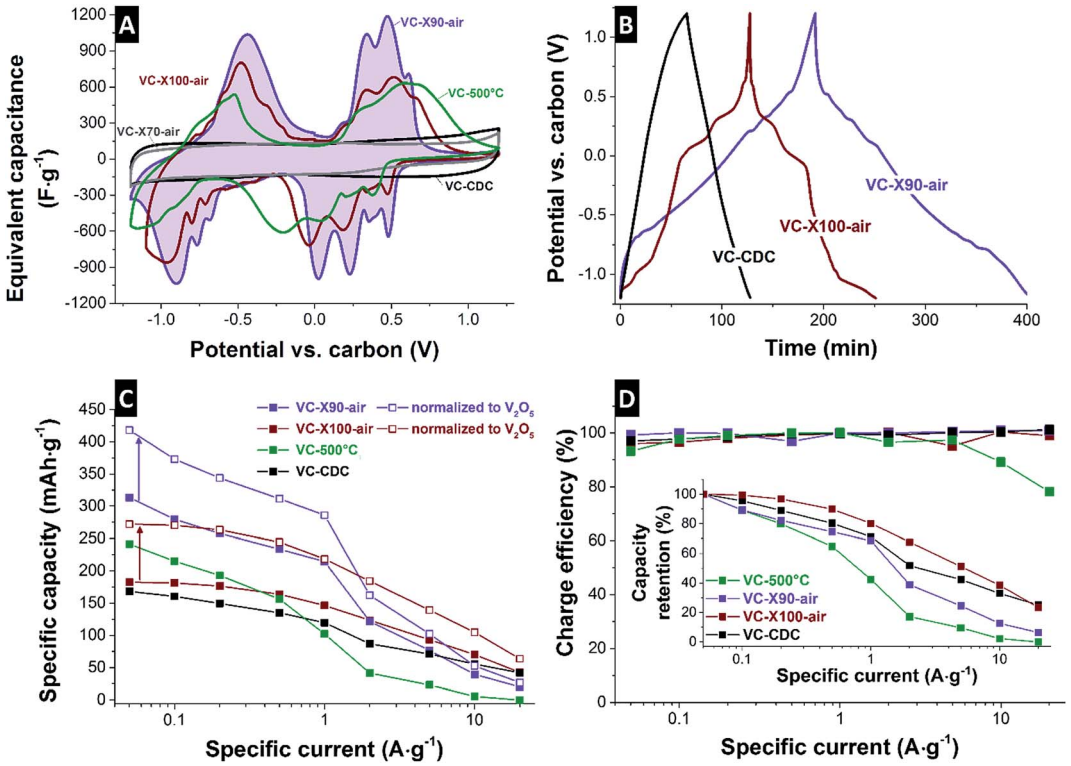

Fig. 4 (A) Cyclic voltammograms at 1 mV s^{-1}, (B) galvanostatic charge–discharge curves at 0.05 A g^{-1}, (C) capacity values dependent on the specific current, and (D) the charge efficiency and capacity retention. All measurements were performed in the half-cell configuration with activated carbon counter and reference electrodes from −1.2 V to +1.2 V *vs.* carbon.

for VC-X90-air with more than 300 mA h g^{-1}. Typically, in the literature capacity values are normalized to the active mass, in this case the mass of V_2O_5 in the composite electrode. Using this way of normalization, the highest capacity for VC-X90-air is 415 mA h g^{-1}. Even for higher specific currents of 5 A g^{-1} the specific capacity reaches more than 100 mA h g^{-1} (comparable to a C-rate of 12C). The normalized values are given as an inset in Fig. 4D for comparison. Cycling in the potential window of −1.2 V to +1.2 V *vs.* carbon is expected to be completely reversible,[48,51,52] and this behavior was confirmed for all V_2O_5/CDC core–shell particles with a coulombic efficiency of *ca.* 100% (Fig. 4D). The VC particles calcined at 500 °C with much larger particle sizes (Fig. 1B) and without CDC shells, present a lower charge efficiency of less than 80% at 20 A g^{-1}. This might be the result of V_2O_5 degeneration due to kinetic limitations.[30]

Electrochemical properties on a device level were measured using an asymmetric full-cell setup with nanoporous VC-CDC as the counter electrode. Typically, symmetric setups for electrode

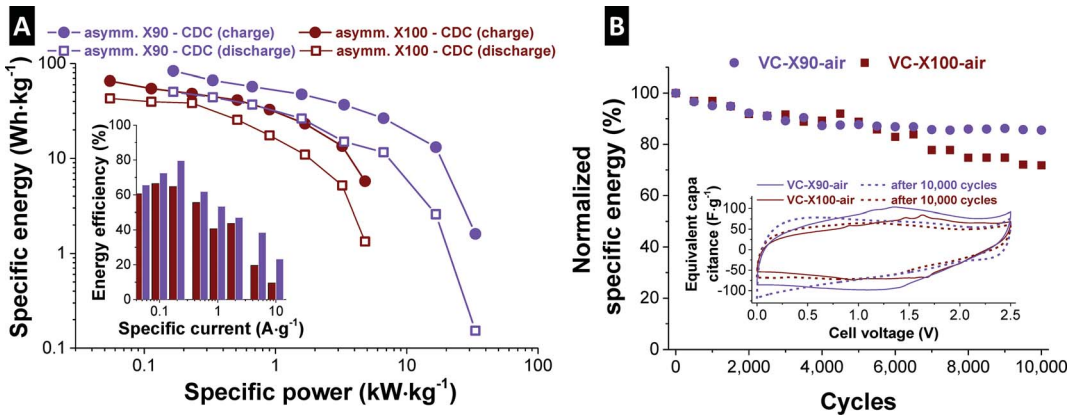

Fig. 5 (A) Ragone plot with energy efficiency values and (B) specific energy retention for 10 000 galvanostatic cycles at 1 A g^{-1} (rate of *ca.* 2.4C) with cyclic voltammograms recorded before and after stability testing. All measurements were performed in the full-cell configuration with a charge-balanced VC-CDC working electrode and V_2O_5/CDC composite electrode with a cell voltage of 2.5 V.

Table 3 Literature values for full-cell measurements (two-electrodes) in symmetric and asymmetric fabrication. OLC: onion-like carbon; CNT: carbon nanotube; NW: nanowire; rGO: reduced graphene oxide; ACC: activated carbon fabric; NS: nanosheet; PPy: polypyrrole; sym.: symmetric; asym.: asymmetric; ACN: acetonitrile; PC: propylene carbonate; LiTFSI: lithium bis(trifluoromethylsulphonyl)imide; WE: working electrode; CE: counter electrode

Material (WE)	Setup	CE	Electrolyte	Specific energy W h kg^{-1}	Specific power W kg^{-1}	Ref.
V_2O_5/CDC core–shell	asym.	CDC	1 M $LiClO_4$ in ACN	84 (51)	166	This study
				27 (12)	6653	
V_2O_5/OLC	asym.	AC	1 M $LiClO_4$ in ACN	38	57	33
				10	2004	
V_2O_5/CNTs	asym.	AC	1 M $LiClO_4$ in PC	40	200	22
				7	6300	
V_2O_5 nanowires	asym.	AC fabric	0.1 M LiTFSI in ACN	46	662	59
				6	5260	
Li^+ exchanged V_2O_5 NWs	asym.	AC fabric	0.1 M LiTFSI in ACN	66	720	59
				7	8320	
V_2O_5 NWs/rGO	asym.	MnO_2/rGO	1 M LiTFSI in ACN	15	437	60
V_2O_5/Pin/ACC	asym.	rGO/ACC	$LiNO_3$/PVA gel	39	900	65
				33	18 000	
V_2O_5/rGO NS	asym.	rGO	1 M KCl	76	900	34
				25	30 000	
$V_2O_5 \cdot 0.6H_2O$	asym.	AC	0.5 M K_2SO_4	29	70	58
				20	2000	
Layered V_2O_5 aerogel	asym.	AC	1 M Na_2SO_4	11	280	66
				5	2200	
V_2O_5/MWCNTs	sym.	WE	1 M Na_2SO_4	87	250	56
V_2O_5 nanofibers	sym.	WE	1 M $LiClO_4$ in PC	78	1800	55
				15	1500	
			2 M KCl	5	1700	55
				3	1800	
V_2O_5/PPy core–shell	sym.	WE	$LiNO_3$/PVA gel	10	5000	67
V_2O_5/graphene	sym.	WE	1 M Na_2SO_4	68	250	57

materials with battery-like behavior (*e.g.*, intercalation/deintercalation) are disadvantageous due to their polarization dependent redox-reactions. Yet, several studies used different types of V_2O_5 or V_2O_5/carbon composites, such as electrospun V_2O_5 nanofibers,[55] V_2O_5/MWCNT core–shell aerogels,[56] and V_2O_5/graphene aerogels[57] with the symmetrical full-cell setup. However, in some of these studies, negative and positive polarization in the full-cell arrangement was used (*e.g.* −1 V to +1 V in an aqueous electrolyte), instead of 0 V to 1 V. In these cases the capacitance and specific energies are much larger reaching misleading high values of 87 W h kg^{-1} in aqueous 1 M Na_2SO_4 (ref. 56) and 78 W h kg^{-1} in organic 1 M $LiClO_4$ in PC.[55]

Enhanced electrochemical performance can be obtained by use of an asymmetric two-electrode setup (Fig. 5). Studies so far have shown, for aqueous systems, the highest specific energy of 29 W h kg^{-1} (Table 3) for hydrothermally prepared $V_2O_5 \cdot 0.6H_2O$ with activated carbon as the counter electrode.[58] Due to the improved voltage stability of organic electrolytes, much higher energies can be achieved, ranging from 15 to 76 W h kg^{-1} with MnO_2/rGO, AC fabric, or rGO as the counter electrode in an asymmetric arrangement.[34,59,60] In this study, an asymmetric full-cell setup with V_2O_5/CDC on the negative polarization side and charge-balanced VC-CDC on the positive polarization side was used. VC-X90-air as a negative electrode material presents superior performance with a specific energy in excess of 80 W h kg^{-1} for charging and more than 50 W h kg^{-1} for discharging (Fig. 5A). Even at higher rates, with a specific power of ~6.7 kW kg^{-1}, the specific energy is 27 W h kg^{-1} (12 W h kg^{-1} for discharging). In agreement with half-cell measurements, VC-X100-air shows a lower specific energy of 66 W h kg^{-1} with comparable power handling because of the lower V_2O_5 content. The energy and power performance of this core–shell system is highly competitive with current literature values and is, to the best of our knowledge, the only core–shell system reaching 50–80 W h kg^{-1} specific energy when using asymmetric full-cell measurements and proper application of the cell voltage.[61]

The high attractiveness of this material for electrochemical energy storage is underlined by the high cycling stability with an energy retention of more than 80% and 70% over 10 000 galvanostatic cycles for VC-X90-air and VC-X100-air, respectively, measured at 1 A g^{-1} (Fig. 5B). The nearly ideal charge efficiency of the half-cell measurements (100%) translates to a still attractive energy efficiency of the asymmetric devices between 60 and 80% for low rates. For comparison, standard double-layer capacitors using activated carbon electrodes only reach slightly higher values of 80–95% dependent on the electrode.[62]

4. Conclusions

This study, for the first time, demonstrates a two-step *in situ* synthesis of hybrid particles consisting of porous carbon and redox-active V_2O_5 by solely using VC as the precursor. The

particles present a V_2O_5/CDC core–shell structure with nanoscopic V_2O_5 cores, completely accessible to electrolyte ions and interconnected by highly conductive carbon. High specific energies of 50 and 80 W h kg^{-1} for discharging and charging, respectively, were measured in a facile asymmetric full-cell setup, while simultaneously retaining ultrafast cycling. The asymmetric cell design with CDC on the positive polarization side leads to superior stability over 10 000 cycles and comparably high energy efficiency of 60–80% at low rates. The novel synthesis procedure can easily be scaled up by means of larger precursor mass and may also be very attractive for other redox-active compounds.

Acknowledgements

M. Z., B. K., and V. P. gratefully acknowledge funding from the German Federal Ministry for Research and Education (BMBF) in support of the nanoEES^{3D} project (award number 03EK3013) as part of the strategic funding initiative energy storage framework and Prof. Eduard Arzt (INM) for his continuing support. T. A., and B. E. gratefully acknowledge the funding of the German Federal Ministry of Education and Research (BMBF) under the project AktivCAPs (award number 02E2-ESP077) and the German Research Council (DFG), which, within the framework of its "Excellence Initiative", supports the Cluster of Excellence "Engineering of Advanced Materials" (http://www.eam.uni-erlangen.de) at the University of Erlangen-Nuremberg. T. A. gratefully acknowledges the Indonesian Directorate General of Higher Education (DIKTI) for a PhD scholarship. Dr Mesut Aslan is thanked for vanadium carbide chlorination.

References

1 P. Simon, Y. Gogotsi and B. Dunn, *Science*, 2014, **343**, 1210–1211.
2 P. Simon and Y. Gogotsi, *Nat. Mater.*, 2008, **7**, 845–854.
3 J. B. Goodenough, *Energy Environ. Sci.*, 2014, **7**, 14–18.
4 Z. Yang, J. Zhang, M. C. Kintner-Meyer, X. Lu, D. Choi, J. P. Lemmon and J. Liu, *Chem. Rev.*, 2011, **111**, 3577–3613.
5 J. R. Miller, *J. Power Sources*, 2016, **326**, 726–735.
6 F. Béguin, V. Presser, A. Balducci and E. Frackowiak, *Adv. Mater.*, 2014, **26**, 2219–2251.
7 N. Jäckel, M. Rodner, A. Schreiber, J. Jeongwook, M. Zeiger, M. Aslan, D. Weingarth and V. Presser, *J. Power Sources*, 2016, **326**, 660–671.
8 V. Presser, M. Heon and Y. Gogotsi, *Adv. Funct. Mater.*, 2011, **21**, 810–833.
9 O. Barbieri, M. Hahn, A. Herzog and R. Kötz, *Carbon*, 2005, **43**, 1303–1310.
10 J. Chmiola, G. Yushin, Y. Gogotsi, C. Portet, P. Simon and P. L. Taberna, *Science*, 2006, **313**, 1760–1763.
11 E. Frackowiak, K. Fic, M. Meller and G. Lota, *ChemSusChem*, 2012, **5**, 1181–1185.
12 B. E. Conway, V. Birss and J. Wojtowicz, *J. Power Sources*, 1997, **66**, 1–14.
13 M. Salanne, B. Rotenberg, K. Naoi, K. Kaneko, P.-L. Taberna, C. Grey, B. Dunn and P. Simon, *Nat. Energy*, 2016, **1**, 16070.
14 J. Lee, B. Krüner, A. Tolosa, S. Sethuraman, D. Kim, S. Choudhury, K. H. Seo and V. Presser, *Energy Environ. Sci.*, 2016, **9**, 3392–3398.
15 T. Brousse, D. Bélanger and J. W. Long, *J. Electrochem. Soc.*, 2015, **162**, A5185–A5189.
16 J. Zheng, P. Cygan and T. Jow, *J. Electrochem. Soc.*, 1995, **142**, 2699–2703.
17 C. Xu, F. Kang, B. Li and H. Du, *J. Mater. Res.*, 2010, **25**, 1421–1432.
18 M. Ghidiu, M. R. Lukatskaya, M.-Q. Zhao, Y. Gogotsi and M. W. Barsoum, *Nature*, 2014, **516**, 78–81.
19 S. Roldán, C. Blanco, M. Granda, R. Menéndez and R. Santamaría, *Angew. Chem., Int. Ed.*, 2011, **50**, 1699–1701.
20 M. Zeiger, D. Weingarth and V. Presser, *ChemElectroChem*, 2015, **2**, 1117–1127.
21 N. Nitta, F. Wu, J. T. Lee and G. Yushin, *Mater. Today*, 2015, **18**, 252–264.
22 Z. Chen, V. Augustyn, J. Wen, Y. Zhang, M. Shen, B. Dunn and Y. Lu, *Adv. Mater.*, 2011, **23**, 791–795.
23 J. S. Daubert, N. P. Lewis, H. N. Gotsch, J. Z. Mundy, D. N. Monroe, E. C. Dickey, M. D. Losego and G. N. Parsons, *Chem. Mater.*, 2015, **27**, 6524–6534.
24 L.-M. Chen, Q.-Y. Lai, Y.-J. Hao, Y. Zhao and X.-Y. Ji, *J. Alloys Compd.*, 2009, **467**, 465–471.
25 T. Kudo, Y. Ikeda, T. Watanabe, M. Hibino, M. Miyayama, H. Abe and K. Kajita, *Solid State Ionics*, 2002, **152–153**, 833–841.
26 D. Chao, X. Xia, J. Liu, Z. Fan, C. F. Ng, J. Lin, H. Zhang, Z. X. Shen and H. J. Fan, *Adv. Mater.*, 2014, **26**, 5794–5800.
27 Y. L. Cheah, V. Aravindan and S. Madhavi, *ACS Appl. Mater. Interfaces*, 2013, **5**, 3475–3480.
28 D. Zhu, H. Liu, L. Lv, Y. D. Yao and W. Z. Yang, *Scr. Mater.*, 2008, **59**, 642–645.
29 M. Sathiya, A. S. Prakash, K. Ramesha, J. M. Tarascon and A. K. Shukla, *J. Am. Chem. Soc.*, 2011, **133**, 16291–16299.
30 Y. Liu, M. Clark, Q. Zhang, D. Yu, D. Liu, J. Liu and G. Cao, *Adv. Energy Mater.*, 2011, **1**, 194–202.
31 M.-S. Balogun, Y. Luo, F. Lyu, F. Wang, H. Yang, H. Li, C. Liang, M. Huang, Y. Huang and Y. Tong, *ACS Appl. Mater. Interfaces*, 2016, **8**, 9733–9744.
32 Q. Xu and T. Zhao, *Prog. Energy Combust. Sci.*, 2015, **49**, 40–58.
33 S. Fleischmann, N. Jäckel, M. Zeiger, B. Krüner, I. Grobelsek, P. Formanek, S. Choudhury, D. Weingarth and V. Presser, *Chem. Mater.*, 2016, **28**, 2082–2813.
34 D. H. Nagaraju, Q. Wang, P. Beaujuge and H. N. Alshareef, *J. Mater. Chem. A*, 2014, **2**, 17146–17152.
35 M. Schmirler, F. Glenk and B. J. Etzold, *Carbon*, 2011, **49**, 3679–3686.
36 T. Ariyanto, B. Dyatkin, G.-R. Zhang, A. Kern, Y. Gogotsi and B. J. Etzold, *Microporous Mesoporous Mater.*, 2015, **218**, 130–136.
37 C. R. Pérez, S. H. Yeon, J. Ségalini, V. Presser, P. L. Taberna, P. Simon and Y. Gogotsi, *Adv. Funct. Mater.*, 2013, **23**, 1081–1089.
38 A. Jänes, T. Thomberg and E. Lust, *Carbon*, 2007, **45**, 2717–2722.

39 J. G. Speight, *Lange's Handbook of Chemistry*, McGraw-Hill, New York, 16 edn, 2005.
40 T. Huang, S. Mao, G. Zhou, Z. Wen, X. Huang, S. Ci and J. Chen, *Nanoscale*, 2014, **6**, 9608–9613.
41 A. Ferrari and J. Robertson, *Phys. Rev. B: Condens. Matter Mater. Phys.*, 2000, **61**, 14095.
42 A. C. Ferrari and J. Robertson, *Phys. Rev. B*, 2001, **64**, 075414.
43 Z. Huang, D. Wang, J. Wen, M. Sennett, H. Gibson and Z. Ren, *Appl. Phys. A: Mater. Sci. Process.*, 2002, **74**, 387–391.
44 R. Baddour-Hadjean, J. P. Pereira-Ramos, C. Navone and M. Smirnov, *Chem. Mater.*, 2008, **20**, 1916–1923.
45 S.-H. Lee, H. M. Cheong, M. J. Seong, P. Liu, C. E. Tracy, A. Mascarenhas, J. R. Pitts and S. K. Deb, *Solid State Ionics*, 2003, **165**, 111–116.
46 G. Petrov, V. Yakovlev and J. Squier, *Appl. Phys. Lett.*, 2002, **81**, 1023–1025.
47 M. Thommes, K. Kaneko, A. V. Neimark, J. P. Olivier, F. Rodriguez-Reinoso, J. Rouquerol and K. S. Sing, *Pure Appl. Chem.*, 2015, **87**, 1051–1069.
48 C. Leger, S. Bach, P. Soudan and J.-P. Pereira-Ramos, *J. Electrochem. Soc.*, 2005, **152**, A236–A241.
49 M. Koltypin, V. Pol, A. Gedanken and D. Aurbach, *J. Electrochem. Soc.*, 2007, **154**, A605–A613.
50 J. Livage, *Chem. Mater.*, 1991, **3**, 578–593.
51 C. Delmas, H. Cognac-Auradou, J. Cocciantelli, M. Menetrier and J. Doumerc, *Solid State Ionics*, 1994, **69**, 257–264.
52 C. Delmas, S. Brethes and M. Menetrier, *J. Power Sources*, 1991, **34**, 113–118.
53 M. S. Whittingham, *Chem. Rev.*, 2004, **104**, 4271–4302.
54 V. Augustyn, P. Simon and B. Dunn, *Energy Environ. Sci.*, 2014, **7**, 1597–1614.
55 G. Wee, H. Z. Soh, Y. L. Cheah, S. G. Mhaisalkar and M. Srinivasan, *J. Mater. Chem.*, 2010, **20**, 6720–6725.
56 Y. Wu, G. Gao, H. Yang, W. Bi, X. Liang, Y. Zhang, G. Zhang and G. Wu, *J. Mater. Chem. A*, 2015, **3**, 15692–15699.
57 Y. Wu, G. Gao and G. Wu, *J. Mater. Chem. A*, 2015, **3**, 1828–1832.
58 Q. T. Qu, Y. Shi, L. L. Li, W. L. Guo, Y. P. Wu, H. P. Zhang, S. Y. Guan and R. Holze, *Electrochem. Commun.*, 2009, **11**, 1325–1328.
59 S. D. Perera, B. Patel, N. Nijem, K. Roodenko, O. Seitz, J. P. Ferraris, Y. J. Chabal and K. J. Balkus, *Adv. Energy Mater.*, 2011, **1**, 936–945.
60 S. D. Perera, M. Rudolph, R. G. Mariano, N. Nijem, J. P. Ferraris, Y. J. Chabal and K. J. Balkus Jr, *Nano Energy*, 2013, **2**, 966–975.
61 M. D. Stoller and R. S. Ruoff, *Energy Environ. Sci.*, 2010, **3**, 1294–1301.
62 A. Laheäär, P. Przygocki, Q. Abbas and F. Béguin, *Electrochem. Commun.*, 2015, **60**, 21–25.
63 T. Ariyanto, A. M. Laziz, J. Gläsel, G.-R. Zhang, J. Garbes and B. J. Etzold, *Chem. Eng. J.*, 2016, **283**, 676–681.
64 S. Brunauer, P. H. Emmett and E. Teller, *J. Am. Chem. Soc.*, 1938, **60**, 11.
65 X. Zhou, Q. Chen, A. Wang, J. Xu, S. Wu and J. Shen, *ACS Appl. Mater. Interfaces*, 2016, **8**, 3776–3783.
66 C. X. Guo, G. Yilmaz, S. Chen, S. Chen and X. Lu, *Nano Energy*, 2015, **12**, 76–87.
67 T. Qian, N. Xu, J. Zhou, T. Yang, X. Liu, X. Shen, J. Liang and C. Yan, *J. Mater. Chem. A*, 2015, **3**, 488–493.